

Optimizing Lead-Free Chalcogenide Perovskites for High-Efficiency Photovoltaics via Alloying Strategies

Surajit Adhikari*, Priya Johari*
Department of Physics, School of Natural Sciences,
Shiv Nadar Institution of Eminence, Greater Noida,
Gautam Buddha Nagar, Uttar Pradesh 201314, India

Lead-free chalcogenide perovskites are emerging as game-changers in the race for sustainable, high-performance photovoltaics. These materials offer a perfect trifecta: non-toxic elemental composition, exceptional phase stability, and outstanding optoelectronic properties. However, unlocking their full potential for solar cell applications requires advanced strategies to fine-tune their electronic and optical behavior. In this study, we take CaHfS_3 —a promising but underexplored candidate—and revolutionize its performance by introducing targeted substitutions: Ti at the cation site and Se at the anion site. Using cutting-edge computational techniques, including density functional theory, GW calculations, and the Bethe-Salpeter equation (BSE), we reveal how these substitutions transform the material's properties. Our findings highlight that alloyed compounds such as $\text{CaHfS}_{3-x}\text{Se}_x$ and $\text{CaHf}_{1-y}\text{Ti}_y\text{X}_3$ ($X = \text{S}, \text{Se}$) are not only phase-stable but also feature adjustable direct G_0W_0 @PBE bandgaps (1.29–2.67 eV), reduced exciton binding energies, and significantly improved polaron mobility. These modifications enable better light absorption, reduced electron-hole recombination, longer exciton lifetimes, and enhanced quantum yield. Impressively, the alloyed perovskites, specifically, for the Ti-rich Se-based perovskites, achieve a spectroscopic-limited maximum efficiency of up to 28.06%, outperforming traditional lead-based halide perovskites. Our results demonstrate that strategic alloying is a powerful tool to supercharge the optoelectronic properties of lead-free chalcogenide perovskites, positioning them as strong contenders for next-generation photovoltaic technologies.

I. INTRODUCTION:

Inorganic–organic halide perovskites (IOHPs) have garnered unparalleled attention over the past decade due to their exceptional electronic and optical properties [1–4]. Consequently, the popularity of IOHPs in solar cell research has skyrocketed in recent years, with their record power conversion efficiency (PCE) increasing dramatically from 3.8% to 26.7% [1, 5]. Despite these advances, a critical challenge persists: the majority of IOHPs are lead (Pb)-based, raising serious concerns about toxicity. Additionally, issues such as degradability, along with thermal and chemical instability attributed to the organic components, present formidable barriers to their large-scale industrial deployment [6, 7]. These challenges have driven research toward designing stable, nontoxic alternative perovskites, paving the way for new, efficient photovoltaic materials.

Recently, chalcogenide perovskites (CPs) materials have garnered significant attention as promising alternatives to lead-based perovskites for solar cell technology [8–11]. The chemical formula of CPs is represented as ABX_3 [11, 12], where A and B correspond to divalent alkali-earth metal cations (Ca^{2+} , Sr^{2+} , Ba^{2+}) and tetravalent transition metal cations (Ti^{4+} , Zr^{4+} , Hf^{4+}), respectively. The X site is typically occupied by a chalcogen anion such as S^{2-} or Se^{2-} . Numerous experimental and theoretical studies have successfully demonstrated the synthesis of CPs, revealing their fascinating and promising properties [8–11, 13–15]. Also, at ambient temperature, two distinct phases of CPs have been identified: a needle-like orthorhombic phase (NH_4CdCl_3 -type) and a distorted orthorhombic structure (GdFeO_3 -type). Despite their structural differences, both phases share the same space group, $Pnma$ (No. 62) [11].

Among these CPs, ABS_3 ($A = \text{Ca}, \text{Sr}, \text{Ba}$; $B = \text{Zr}, \text{Hf}$) have been experimentally synthesized with distorted structures featuring corner-sharing BS_6 octahedra connected in a three-dimensional network [15]. Also, a distorted CaTiS_3 CP has been recently synthesized experimentally, exhibiting a bandgap of 1.59 eV [16]. In addition, several first-principles-based studies have predicted that ABX_3 ($A = \text{Ca}, \text{Sr}, \text{Ba}$; $B = \text{Zr}, \text{Hf}$ and $X = \text{S}, \text{Se}$) CPs exhibit promising electronic and optical properties, making them attractive for optoelectronic applications [14, 17, 18]. However, the performance of ABS_3 ($A = \text{Ca}, \text{Sr}, \text{Ba}$; $B = \text{Zr}, \text{Hf}$) CPs in photovoltaic applications is significantly hindered compared to conventional lead-based HPs [19–25], due to their higher bandgaps (1.83–2.46 eV), large exciton binding energies (0.19–0.26 eV), lower charge carrier mobilities (6.84 – $18.77 \text{ cm}^2\text{V}^{-1}\text{s}^{-1}$), and reduced PCE (10.56–25.02%) [14, 15, 17]. Another study shows that selenide-based CPs outperform sulfur-based CPs in photovoltaic properties

* sa731@snu.edu.in, priya.johari@snu.edu.in

[18]. However, their performance remains inferior to that of lead-based conventional HPs, with lower charge carrier mobilities ($56.08\text{--}77.59\text{ cm}^2\text{V}^{-1}\text{s}^{-1}$) and reduced PCE ($17.45\text{--}23.08\%$). Therefore, it is essential to investigate CPs with optimal photovoltaic properties to address these challenges effectively.

It is well-known that the BX_6 octahedra, which form the core of ABX_3 perovskite materials, play a crucial role in determining the material's electronic band structure, influencing properties such as the bandgap, charge carrier mobility, and efficiency. Recently, several studies have focused on tuning the electronic structure of CPs by chemically substituting cations or anions at the B and X sites. For instance, Meng et al. demonstrated a significant reduction in the bandgap of BaZrS_3 through first-principles simulations by alloying Ti with Zr. They reported that doping the perovskite ($\text{BaZr}_{1-x}\text{Ti}_x\text{S}_3$, $x = 0.1$) reduced the bandgap to 1.47 eV, making it suitable for single-junction solar cell applications [26]. Similarly, several experimental and first-principles-based studies have shown that alloying in CPs, such as $\text{BaHf}_{1-x}\text{Ti}_x\text{S}_3$ ($0 \leq x \leq 0.05$) [27], $\text{BaHf}_{1-x}\text{Zr}_x\text{S}_3$ ($x \leq 1$) [28], and $\text{BaZr}_{1-x}\text{Sn}_x\text{S}_3$ ($x \leq 0.25$) [29], significantly enhances their photovoltaic properties. Liu et al. also explored anion-site engineering in Hf-based CPs to tailor their optoelectronic properties and enhance their photovoltaic performance [30]. However, the excitonic and polaronic properties of the above mentioned mixed and alloyed CPs have not been explored for efficient solar cell applications, largely due to the substantial computational demands.

Inspired by the alloying strategies in CPs for designing efficient materials for optoelectronic applications, this study takes a systematic leap into designing next-gen materials for high-performance optoelectronic applications. We delve into the comprehensive study on the electronic, optical, transport, excitonic, and polaronic properties of $\text{CaHfS}_{3-x}\text{Se}_x$ ($x = 0, 1, 2, 3$) and $\text{CaHf}_{1-y}\text{Ti}_y\text{X}_3$ ($y = 0, 0.25, 0.50, 0.75, 1$; $\text{X} = \text{S}$ and Se) compounds within the framework of density functional theory (DFT) [31, 32] and many-body perturbation theory (MBPT) [33, 34]. Our findings are electrifying: these CPs exhibit direct $\text{G}_0\text{W}_0\text{@PBE}$ [35, 36] bandgaps in the ideal range of 1.29–2.67 eV, setting the stage for exceptional optoelectronic performance. Leveraging the Bethe-Salpeter equation (BSE) method [37, 38], we calculated exciton binding energies (E_B) between 0.008 and 0.204 eV, ensuring robust excitonic stability. Adding depth, we employed density functional perturbation theory (DFPT) [39] to assess ionic contributions to dielectric behavior, followed by the Fröhlich and Hellwarth models to explore polaronic phenomena. Our findings indicate that these CPs exhibit carrier-phonon coupling paired with remarkably high polaron mobility, far outpacing traditional lead-based CPs. Pushing boundaries further, we evaluated the spectroscopic limited maximum efficiency (SLME), revealing an impressive potential efficiency of up to 28.06%—a breakthrough for solar cell technology. These results underscore the power of alloying as a game-changing strategy to fine-tune the optoelectronic properties of CPs, paving the way for more efficient, sustainable, and lead-free alternatives in energy applications. This work highlights the transformative potential of alloying to unlock high-efficiency materials and sets a new benchmark for the future of optoelectronics.

II. COMPUTATIONAL DETAILS:

In this paper, state-of-the-art calculations based on first-principles density functional theory (DFT) [31, 32], density functional perturbation theory (DFPT) [39], and many-body perturbation theory (MBPT) [33, 34] were conducted using the Vienna Ab initio Simulation Package (VASP) [40, 41]. The interactions between the valence electrons and the ion cores were described using projector augmented wave (PAW) pseudopotentials [42]. The PAW potentials with valence-electron configurations considered for Ca, Ti, Hf, S, and Se were $3s^23p^64s^2$, $3p^64s^23d^2$, $5p^66s^25d^2$, $3s^23p^4$, and $4s^24p^4$, respectively. The structural optimizations were performed using the Perdew-Burke-Ernzerhof (PBE) exchange-correlation (xc) functional within the generalized gradient approximation (GGA) [43], which accounts for electron-electron interactions. The kinetic energy cutoff was set to 400 eV and the electronic self-consistent-field iteration energy convergence criteria was chosen at 10^{-6} eV. The lattice parameters as well as coordinates of all the atoms are fully optimized until the Hellmann-Feynman forces on each atom's were less than $0.01\text{ eV}/\text{\AA}$. In order to determine the optimized structures, Brillouin zone integrations were performed using a $7 \times 7 \times 5$ Γ -centered \mathbf{k} -point grid. The optimized crystal structures were visualized using the VESTA (Visualization for Electronic and Structural Analysis) software [44]. The phonon dispersion curves were computed using the DFPT method with $2 \times 2 \times 2$ supercells, employing the PHONOPY package [45]. The electronic band structures were computed using the PBE xc functional, incorporating the spin-orbit coupling (SOC) effect, although it does not influence the overall trend. In addition, the electronic bandgaps were simultaneously calculated using the hybrid HSE06 xc functional [46] and the MBPT-based G_0W_0 method [35, 36] for more accurate estimation. The initial step of the G_0W_0 calculation was carried out using the PBE xc functional. The effective masses of the charge carriers were estimated using the SUMO code, which performed a parabolic fitting at the band edges. The Bethe-Salpeter equation (BSE) [37, 38] calculations were also performed on top of the single-shot GW (G_0W_0)@PBE to more accurately estimate the optical properties, specifically incorporating the electron-hole interaction. Here, a Γ -centered $3 \times 3 \times 2$ \mathbf{k} -grid and a converged number of bands (NBANDS) of 640 were used for the GW-BSE calculations. The electron-hole kernel for the BSE

calculations was generated using 24 occupied and 24 unoccupied bands. The VASPKIT [47] package was employed for the post-processing of the elastic and optical properties. The ionic contribution to the dielectric constant was also determined using the DFPT method.

Using the hydrogenic Wannier-Mott (WM) model, the exciton binding energy (E_B) for an electron-hole pair with screened Coulomb interaction is calculated as follows [18, 48]:

$$E_B = \left(\frac{\mu^*}{m_0 \varepsilon_{\text{eff}}^2} \right) R_\infty \quad (1)$$

where μ^* is the reduced mass of the charge carriers, m_0 represents the rest mass of electron, ε_{eff} denotes the effective dielectric constant, and R_∞ is the Rydberg constant. The effective mass has been determined using the following equation [49]:

$$m^* = 3 \left[\frac{1}{m_{xx}^*} + \frac{1}{m_{yy}^*} + \frac{1}{m_{zz}^*} \right]^{-1} \quad (2)$$

where m_{ii}^* is the effective mass in the i -th direction ($i = x, y, z$). The reduced mass of the carrier, μ^* , is given by,

$$\frac{1}{\mu^*} = \frac{1}{m_e^*} + \frac{1}{m_h^*}. \quad (3)$$

The correction to the exciton binding energy (E_B) due to phonon screening is expressed as [50]:

$$\Delta E_B^{ph} = -2\omega_{LO} \left(1 - \frac{\varepsilon_\infty}{\varepsilon_{\text{static}}} \right) \frac{\sqrt{1 + \omega_{LO}/E_B} + 3}{\left(1 + \sqrt{1 + \omega_{LO}/E_B} \right)^3}, \quad (4)$$

where ω_{LO} denotes the characteristic phonon angular frequency, and ε_∞ and $\varepsilon_{\text{static}}$ represent the electronic (optical) and static (electronic + ionic) dielectric constants, respectively. The thermal "B" approach developed by Hellwarth et al. [51] is employed to determine ω_{LO} by averaging the spectral contributions of multiple phonon branches (for details, see the Supplemental Material).

The exciton radius (r_{exc}) is computed using the following formula [18, 48]:

$$r_{exc} = \frac{m_0}{\mu^*} \varepsilon_{\text{eff}} n^2 r_{Ry}, \quad (5)$$

where n represents the exciton energy level and $r_{Ry} = 0.0529$ nm is the Bohr radius. In our study, the electronic contribution to the dielectric function (ε_∞) is taken as the effective value and $n = 1$, which yields the smallest exciton radius. Using the exciton radius, the probability of the wave function at zero separation ($|\phi_n(0)|^2$) can be calculated as follows [18, 52]:

$$|\phi_n(0)|^2 = \frac{1}{\pi (r_{exc})^3 n^3}. \quad (6)$$

Within the framework of Fröhlich's polaron model, the interaction between longitudinal optical phonons and an electron traveling through the lattice is governed by the dimensionless Fröhlich parameter, α , which is expressed as [18],

$$\alpha = \frac{1}{4\pi\varepsilon_0} \frac{1}{2} \left(\frac{1}{\varepsilon_\infty} - \frac{1}{\varepsilon_{\text{static}}} \right) \frac{e^2}{\hbar\omega_{LO}} \left(\frac{2m^*\omega_{LO}}{\hbar} \right)^{1/2} \quad (7)$$

where ε_0 represents the permittivity of free space and m^* denotes the effective mass of the carrier. By determining the value of α , the polaron energy (E_p) can be calculated using the following expression [18]:

$$E_p = (-\alpha - 0.0123\alpha^2)\hbar\omega_{LO}. \quad (8)$$

Using Feynman's approach, the polaron's effective mass (m_p) can be expressed as follows (for a small α) [53]:

$$m_p = m^* \left(1 + \frac{\alpha}{6} + \frac{\alpha^2}{40} + \dots \right) \quad (9)$$

Finally, the polaron mobility (μ_p) is estimated using the Hellwarth polaron model [51] as follows:

$$\mu_p = \frac{(3\sqrt{\pi}e)}{2\pi c\omega_{LO}m^*\alpha} \frac{\sinh(\beta/2)}{\beta^{5/2}} \frac{w^3}{v^3} \frac{1}{K(a,b)} \quad (10)$$

where e denotes the electronic charge, $\beta = hc\omega_{LO}/k_B T$, w and v both are the temperature-dependent variational parameters, and $K(a,b)$ is a function of β , w , and v (for details, see the Supplemental Material).

III. RESULTS AND DISCUSSIONS:

In this present study, we conducted a comprehensive investigation to evaluate the effects of doping in both the cationic and anionic sites on the optoelectronic properties of CaHfS_3 chalcogenide perovskite. The following sections provide an in-depth analysis of the stability, structural and electronic properties, transport behavior, optical properties, excitonic dynamics, polaronic effects, and the spectroscopic limited maximum efficiency (SLME) of $\text{CaHfS}_{3-x}\text{Se}_x$ ($x = 0, 1, 2, 3$) and $\text{CaHf}_{1-y}\text{Ti}_y\text{X}_3$ ($y = 0, 0.25, 0.50, 0.75, 1$; $X = \text{S}$ and Se) chalcogenide perovskites. These findings aim to build a fundamental understanding and provide valuable insights to guide future experimental investigations.

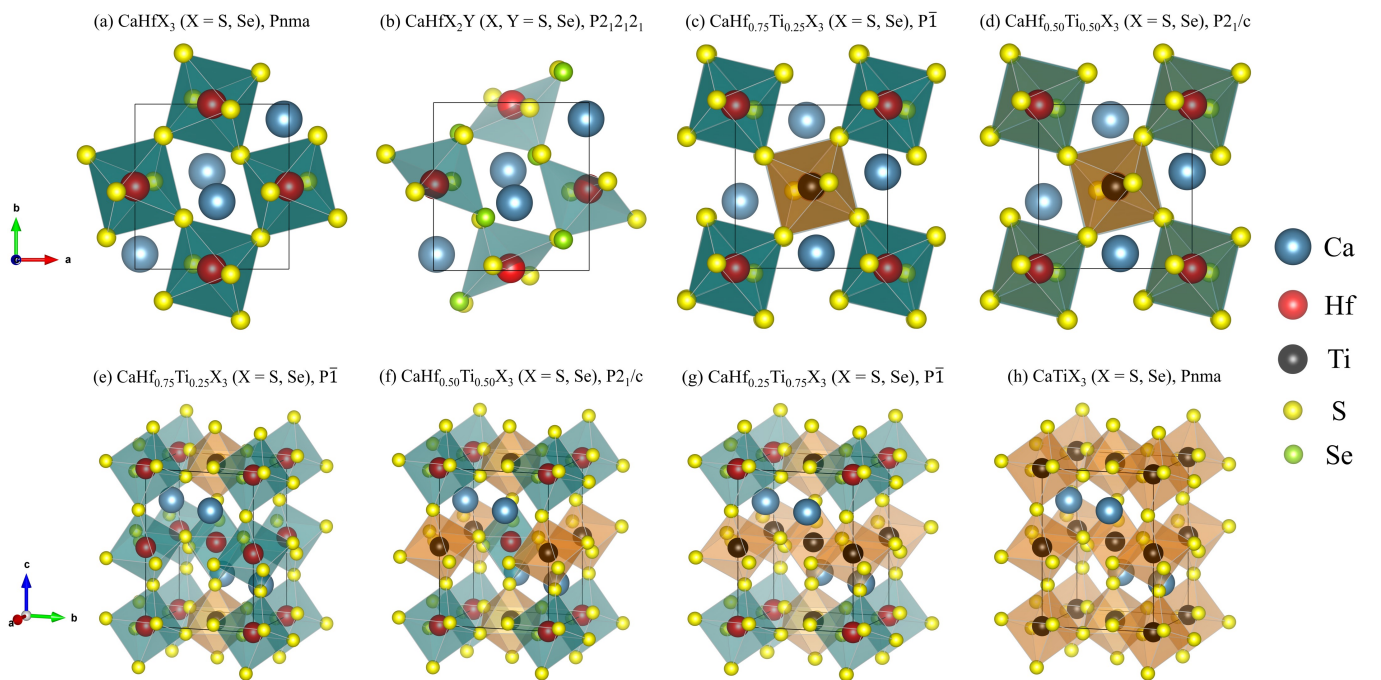


Figure 1. Different view of the crystal structures of (a) CaHfX_3 ($X=\text{S}, \text{Se}$), (b) $\text{CaHfX}_2\text{Y}/\text{XY}_2$ ($X, Y=\text{S}, \text{Se}; X \neq Y$), (c, e) $\text{CaHf}_{0.75}\text{Ti}_{0.25}\text{X}_3$ ($X=\text{S}, \text{Se}$), (d, f) $\text{CaHf}_{0.50}\text{Ti}_{0.50}\text{X}_3$ ($X=\text{S}, \text{Se}$), (g) $\text{CaHf}_{0.25}\text{Ti}_{0.75}\text{X}_3$ ($X=\text{S}, \text{Se}$), and (h) CaTiX_3 ($X=\text{S}, \text{Se}$) CPs, respectively.

A. Structural Properties:

1. Crystal structure and crystallographic stability:

Figure 1(a) illustrates the crystal structure of the distorted orthorhombic phase of the chalcogenide perovskite CaHfX_3 ($X = \text{S}, \text{Se}$), which belongs to the space group $Pnma$ (No. 62). The crystal structures of these compounds typically consist of four unit cells containing a total of 20 atoms, including 4 Ca, 4 Hf, and 12 S/Se atoms. In the distorted phase, Ca cation exhibits 12-fold coordination, forming cuboctahedral structures with chalcogenides X (S or Se). Meanwhile, the Hf cation undergoes 6-fold coordination with chalcogen atoms X (S or Se), resulting in the formation of corner-sharing $[\text{HfX}_6]^{8-}$ distorted octahedra, characterized by tilting and structural distortion. To form mixed CP $\text{CaHfS}_{3-x}\text{Se}_x$, sulfur atoms are progressively substituted by selenium atoms. Similarly, in the alloy

$\text{CaHf}_{1-y}\text{Ti}_y\text{X}_3$, hafnium atoms are partially replaced by titanium atoms. The crystal structure of $\text{CaHfS}_{3-x}\text{Se}_x$ ($x = 1, 2$) transitions to a lower-symmetry orthorhombic structure [space group $P2_12_12_1$ (19)] when one chalcogenide site is replaced by another. Similarly, the crystal structures of $\text{CaHf}_{1-y}\text{Ti}_y\text{X}_3$ alloys undergo symmetry reduction when hafnium is partially substituted by titanium. For $y = 0.25$ or 0.75 , the structures reduce to a triclinic phase [space group $P\bar{1}$ (2)], while for $y = 0.50$, they adopt a monoclinic phase [space group $P2_1/c$ (14)]. When $y = 1$, where hafnium is fully replaced by titanium, the structure transitions back to a higher-symmetry orthorhombic phase [space group $Pnma$ (62)]. These systems are modeled using their primitive cell, comprising 20 atoms. The primitive crystal structures of $\text{CaHfS}_{3-x}\text{Se}_x$ ($x = 1, 2$) and $\text{CaHf}_{1-y}\text{Ti}_y\text{X}_3$ ($y = 0.25, 0.5, 0.75, 1$; $X = \text{S, Se}$) CPs are also presented in Figure 1(b)-(h).

The calculated lattice parameters, space group (no.), and volume of the mixed and alloyed CPs are presented in Table I. Notably, the computed lattice parameters for CaHfS_3 show excellent agreement with the available experimental result ($a = 6.52 \text{ \AA}$, $b = 6.98 \text{ \AA}$, $c = 9.54 \text{ \AA}$) [15]. It is also observed that the lattice parameters and volume of these mixed CPs increase with higher selenium content, attributed to the larger ionic radius of Se (1.98 \AA) compared to S (1.84 \AA). Conversely, in alloyed CPs with higher titanium content, the lattice parameters and volume decrease due to the smaller ionic radius of Ti (0.605 \AA) compared to Hf (0.71 \AA). In addition, the octahedral distortion parameters, including the average bond length, bond angle variance, polyhedral volume, and distortion index (bond length) for the HfX_6 and TiX_6 octahedra in $\text{CaHf}_{1-y}\text{Ti}_y\text{X}_3$ ($y = 0, 0.25, 0.5, 0.75, 1$; $X = \text{S, Se}$) CPs, are computed and presented in Table S1. A very low distortion index for the HfX_6 and TiX_6 octahedra in these CPs suggests that the octahedra remain nearly ideal across the composition range, leading to enhanced structural stability, uniform electronic behavior, and predictable optoelectronic properties. This is beneficial for applications where consistent and tunable properties are essential, such as optoelectronic devices.

Table I. Calculated lattice parameters, space group (no.), volume, and decomposition energy of $\text{CaHfS}_{3-x}\text{Se}_x$ ($x = 0, 1, 2, 3$) and $\text{CaHf}_{1-y}\text{Ti}_y\text{X}_3$ ($y = 0, 0.25, 0.5, 0.75, 1$; $X = \text{S, Se}$) CPs.

Configurations	Lattice Parameters (\AA)			Space group (No.)	Volume (\AA^3)	$E_d(\text{B})$ (eV/atom)	$E_d(\text{T})$ (eV/atom)
	a	b	c				
CaHfS_3	6.56	7.01	9.58	$Pnma$ (62)	440.87	-0.0365	-
CaHfS_2Se	6.68	7.19	9.61	$P2_12_12_1$ (19)	460.96	-0.0617	0.0001
CaHfSSe_2	6.79	7.28	9.74	$P2_12_12_1$ (19)	481.45	-0.0423	0.0063
CaHfSe_3	6.84	7.34	10.03	$Pnma$ (62)	504.27	-0.0739	-
$\text{CaHf}_{0.75}\text{Ti}_{0.25}\text{S}_3$	6.51	6.96	9.51	$P\bar{1}$ (2)	431.49	-0.0491	-0.0048
$\text{CaHf}_{0.75}\text{Ti}_{0.25}\text{Se}_3$	6.79	7.29	9.96	$P\bar{1}$ (2)	493.72	-0.0846	-0.0039
$\text{CaHf}_{0.50}\text{Ti}_{0.50}\text{S}_3$	6.47	6.90	9.43	$P2_1/c$ (14)	421.37	-0.0568	-0.0048
$\text{CaHf}_{0.50}\text{Ti}_{0.50}\text{Se}_3$	6.75	7.24	9.89	$P2_1/c$ (14)	483.76	-0.0911	-0.0038
$\text{CaHf}_{0.25}\text{Ti}_{0.75}\text{S}_3$	6.42	6.86	9.36	$P\bar{1}$ (2)	411.86	-0.2184	-0.0051
$\text{CaHf}_{0.25}\text{Ti}_{0.75}\text{Se}_3$	6.71	7.19	9.81	$P\bar{1}$ (2)	473.70	-0.0982	-0.0041
CaTiS_3	6.38	6.79	9.27	$Pnma$ (62)	402.07	-0.0676	-
CaTiSe_3	6.67	7.13	9.74	$Pnma$ (62)	463.27	-0.1007	-

As the structural stability of perovskites plays a pivotal role in determining their suitability for high-performance device applications, we have evaluated the crystallographic stability of these materials. The crystallographic stability of mixed and alloyed perovskites has been analyzed by calculating Goldschmidt's tolerance factor (t) [54, 55] and the octahedral factor (μ) [55, 56] (for details, see the Supplemental Material). The calculated values of t and μ are presented in Table S2, ranging from 0.873–0.920 and 0.306–0.386, respectively, confirming the stability of the investigated perovskites.

2. Thermodynamic stability:

To evaluate the thermodynamic stability of the mixed and alloyed CPs, their decomposition energies are calculated using the PBE xc functional. In our study, the stability of $\text{CaHfS}_{3-x}\text{Se}_x$ and $\text{CaHf}_{1-y}\text{Ti}_y\text{X}_3$ compounds is estimated by calculating the energies needed to decompose them into their binary phases, such as CaX , HfX_2 , and TiX_2 , or into ternary phases like CaHfX_3 and CaTiX_3 (for details, see the Supplemental Material). The positive decomposition energies (E_d) indicate that these compounds will remain stable and will not break down into their respective binary (B) or ternary (T) phases. As shown in Table I, the compounds CaHfS_2Se and CaHfSSe_2 do not decompose into ternary phases at 0 K, while the remaining compounds have a high possibility of decomposing into both phases at 0 K. Notably, the probability of decomposition into binary phases is considerably higher than that into ternary phases at 0 K. Nevertheless, there is still a chance for these compounds to stabilize at elevated temperatures, as exemplified

by the successful synthesis of CaTiS_3 perovskite at 600-900 $\text{\AA}^\circ\text{C}$ in a vacuum [16], suggesting their potential for higher temperature stability. In our study, thermodynamic stability does not ensure the stability of these materials; thus, we also assess their dynamical and mechanical stability.

3. Dynamical stability:

The dynamical stability of the investigated CPs is also evaluated, as it is a critical factor in determining material stability, directly related to the behavior of phonon modes. To assess this, self-consistent phonon calculations are performed using the DFPT method [39]. The phonon dispersion curves of $\text{CaHfS}_{3-x}\text{Se}_x$ ($x = 0, 1, 2, 3$), shown in Figure 2(a)-(d), indicate that these compounds are dynamically stable at 0 K. The remaining compounds are found to be unstable at 0 K; however, they may achieve dynamical stability at higher temperatures, as discussed before. For $\text{CaHfS}_{3-x}\text{Se}_x$ ($x = 0, 1, 2, 3$) perovskites, the structural symmetry results in 60 phonon modes corresponding to 20 atoms. Of these, 3 are acoustic, while the remaining 57 are optical, categorized as low- and high-frequency phonons, respectively. Notably, the highest optical frequency decreases significantly with increasing Se (x) concentration.

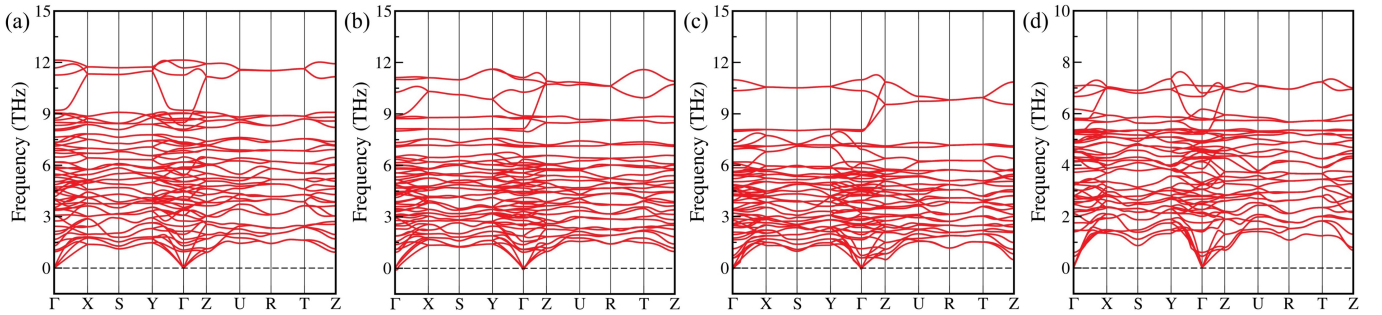


Figure 2. Phonon dispersion curves of (a) CaHfS_3 , (b) CaHfS_2Se , (c) CaHfSSe_2 , and (d) CaHfSe_3 CPs, respectively, calculated with the DFPT method.

4. Mechanical stability and elastic properties:

To assess the mechanical stability of these CPs, the second-order elastic coefficients (C_{ij}) are calculated using the energy-strain approach [57] (for details, see the Supplemental Material). Since the CPs examined in this study belong to different crystal symmetry classes, they exhibit varying numbers of independent elastic constants. The calculated C_{ij} values for these compounds are presented in Table S4 of the Supplemental Material, and they satisfy the Born stability criteria [57]. This certifies the mechanical stability of these alloyed chalcogenide perovskites. The bulk modulus (B), shear modulus (G), Young's modulus (Y), and Poisson's ratio (ν) of all these materials are also determined using their respective elastic coefficients [58, 59], and are presented in Table S5 of the Supplemental Material. Our estimated values for B are significantly higher than those for G in all cases, indicating a stronger resistance to volumetric deformation compared to shape deformation. The lower G values reflect the flexibility of the materials. The fragility of the materials is assessed using Pugh's ratio (B/G) and Poisson's ratio (ν) [60]. The computed values of B/G (> 1.75) and ν (> 0.26) indicate that the investigated CPs exhibit ductile behavior, with the exceptions of CaHfSSe_2 and CaTiSe_3 , which are found to be brittle. These particular mechanical properties make the selected CPs well-suited for use in flexible and durable devices.

B. Electronic properties:

After ensuring the stability of these CPs, electronic structure calculations are performed, as this is crucial for designing photoelectric devices. Therefore, the electronic density of states (DOS), as well as band structures and their nature, are evaluated to provide deep insights into the electronic structure.

Initially, electronic structure calculations for these alloyed CPs are carried out using the widely adopted semilocal PBE xc functional, both with and without including spin-orbit coupling (SOC) effects. However, it is well-established that PBE underestimates the bandgap of chalcogenide perovskites due to self-interaction error [14, 17, 18]. Additionally, our results indicate that SOC has a minimal effect on bandgaps (see Table S5 of the Supplemental Material).

Therefore, the hybrid HSE06 xc functional, along with the MBPT-based $G_0W_0@PBE$ method, has been utilized for precise bandgap estimation of these CPs. The band structures of these compounds, as calculated using HSE06 and $G_0W_0@PBE$, are shown in Figure 3 and Figure S2, respectively. It is observed that all compounds exhibit a direct bandgap, as both the conduction band minimum (CBM) and valence band maximum (VBM) are located at the same k -point, specifically at the Γ -point in the Brillouin zone. It is noteworthy that $CaTiSe_3$ exhibits a slightly indirect bandgap, only 10 meV smaller than the direct bandgap, attributed to the pronounced octahedral tilting of the $TiSe_6$ units. The bandgaps of these CPs, estimated using different functionals/methods, are presented in Table II and show a close agreement with previous theoretical predictions and available experimental data. For example, the $G_0W_0@PBE$ bandgap of $CaTiS_3$ is 1.83 eV, which closely matches its experimental bandgap of 1.59 eV [16]. The difference in bandgap values may be due to temperature, as the experimental measurement was taken at 600 Å °C in a vacuum. The direct bandgaps of these CPs, calculated using HSE06 and $G_0W_0@PBE$, fall within the ranges of 0.69–2.32 eV and 1.29–2.67 eV, respectively. The bandgaps of these alloyed CPs indicate their suitability for photovoltaic applications, aligning closely with those of conventional lead-based HPs (1.50–3.13 eV) [19, 20, 22].

Table II. Bandgap (in eV) of CPs calculated using the PBE, HSE06, and $G_0W_0@PBE$ method, respectively, as well as computed effective mass of electron (m_e^*) and hole (m_h^*) and reduced mass (μ^*) average along the high-symmetry path Γ –X, Γ –Y, and Γ –Z directions. Here, t , e , i , and d represent theoretical, experimental, indirect, and direct bandgaps, respectively, and all values of the effective mass are in terms of free-electron mass (m_0).

Configurations	PBE	HSE06	$G_0W_0@PBE$	Previous Work	$m_e^* (m_0)$	$m_h^* (m_0)$	$\mu^* (m_0)$
$CaHfS_3$	1.52	2.32	2.67	2.46 _t [14]	0.431	0.380	0.202
$CaHfS_2Se$	1.34	2.11	2.39		0.420	0.370	0.197
$CaHfSSe_2$	1.15	1.86	2.09		0.361	0.309	0.166
$CaHfSe_3$	1.05	1.75	1.92		0.358	0.274	0.155
$CaHf_{0.75}Ti_{0.25}S_3$	0.80	1.61	2.48		0.552	0.347	0.213
$CaHf_{0.75}Ti_{0.25}Se_3$	0.43	1.15	1.89		0.444	0.243	0.157
$CaHf_{0.50}Ti_{0.50}S_3$	0.72	1.50	2.34		0.463	0.312	0.186
$CaHf_{0.50}Ti_{0.50}Se_3$	0.37	1.02	1.64		0.345	0.202	0.127
$CaHf_{0.25}Ti_{0.75}S_3$	0.46	1.20	1.99		0.406	0.273	0.163
$CaHf_{0.25}Ti_{0.75}Se_3$	0.16	0.79	1.49		0.277	0.160	0.101
$CaTiS_3$	0.35	1.05	1.83	1.59 _e [16]	0.264	0.224	0.121
$CaTiSe_3$	0.07 ⁱ (0.08 ^d)	0.66 ⁱ (0.69 ^d)	1.17 ⁱ (1.29 ^d)		0.162	0.103	0.063

Furthermore, the variation in bandgap for the mixed $CaHfS_{3-x}Se_x$ ($x = 0, 1, 2, 3$) and alloyed $CaHf_{1-y}Ti_yX_3$ ($y = 0, 0.25, 0.5, 0.75, 1$; $X = S, Se$) CPs as a function of x and y is shown in Figure 4 and fitted for $G_0W_0@PBE$ method. It is observed that the bandgap of these compounds decreases linearly as the values of x (Se) and y (Ti) increase, with deviations of 255 meV, 868 meV, and 664 meV for $CaHfS_{3-x}Se_x$, $CaHf_{1-y}Ti_yS_3$, and $CaHf_{1-y}Ti_ySe_3$, respectively. These trends may aid in predicting the bandgap of mixed and alloyed compounds with different x and y values, which is often encountered during the synthesis of these materials [27, 61].

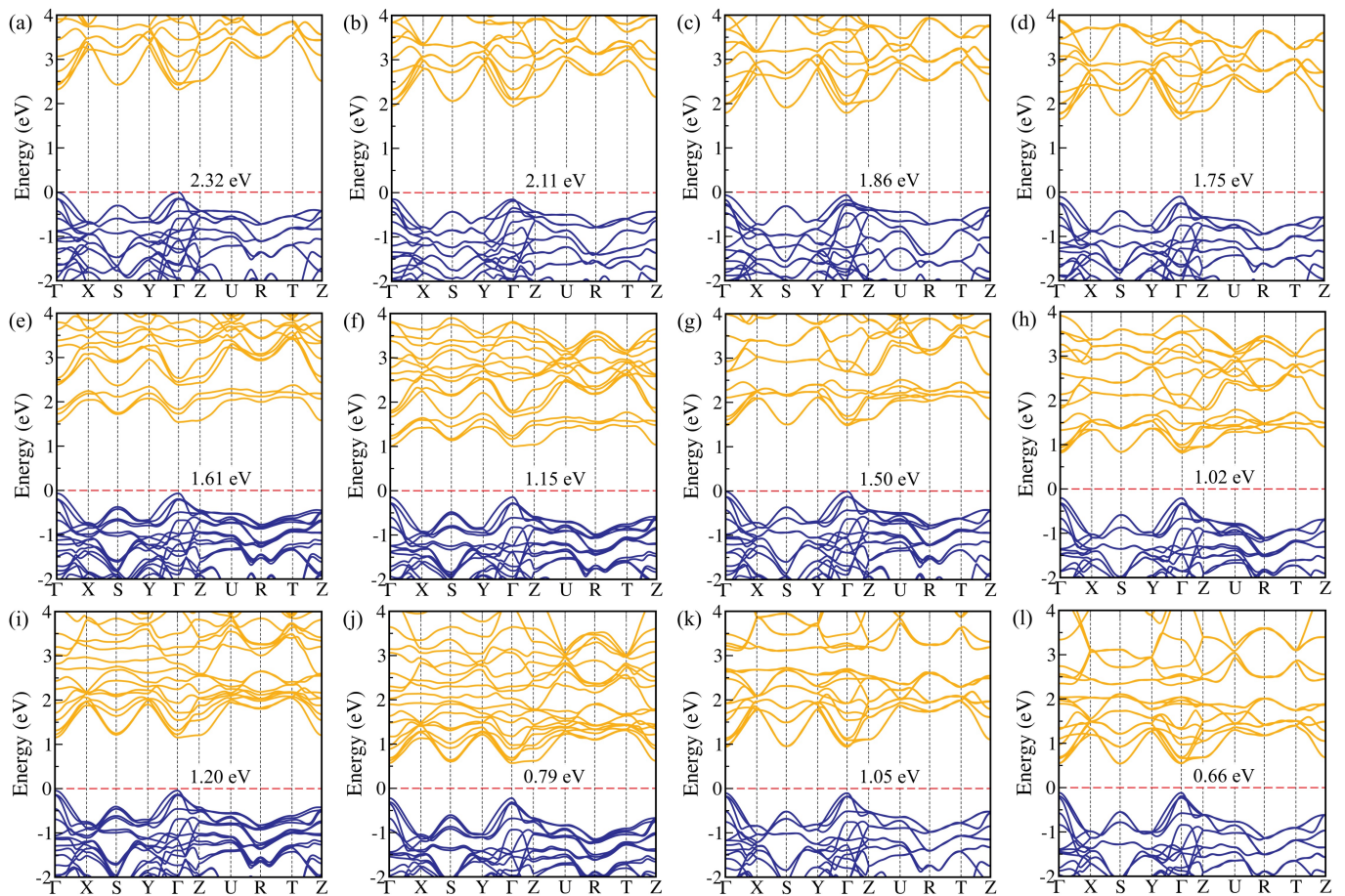


Figure 3. Electronic band structures of [(a)-(d)] $\text{CaHfS}_{3-x}\text{Se}_x$ ($x = 0, 1, 2, 3$), [(e)-(f)] $\text{CaHf}_{0.75}\text{Ti}_{0.25}\text{X}_3$ ($\text{X} = \text{S}, \text{Se}$), [(g)-(h)] $\text{CaHf}_{0.50}\text{Ti}_{0.50}\text{X}_3$ ($\text{X} = \text{S}, \text{Se}$), [(i)-(j)] $\text{CaHf}_{0.25}\text{Ti}_{0.75}\text{X}_3$ ($\text{X} = \text{S}, \text{Se}$), and [(k)-(l)] CaTiX_3 ($\text{X} = \text{S}, \text{Se}$) CPs, respectively, obtained using the HSE06 xc functional. The Fermi level is set to be zero and marked by the dashed line.

To provide a more comprehensive analysis of the electronic band structures of these alloyed compounds, both the total (TDOS) and partial (PDOS) density of states have been calculated using the HSE06 xc functional. The results are illustrated in Figure S1 of the Supplemental Material. For CaHfS_3 , the VBM primarily consists of the S-3p orbitals with a small contribution from Hf-5d orbitals, whereas the CBM is predominantly derived from the Hf-5d orbitals with a minor contribution from S-3p orbitals. Similarly, as the Se content increases in $\text{CaHfS}_{3-x}\text{Se}_x$, the contribution of Se-4p orbitals becomes more significant compared to S-3p orbitals. Since the S-3p orbitals are at a lower energy level than the Se-4p orbitals, the higher energy of the Se-4p orbitals reduces the energy difference between the VBM (primarily Se-4p) and the CBM. This leads to a decrease in bandgap as the Se content increases in $\text{CaHfS}_{3-x}\text{Se}_x$ compounds. Conversely, when the Ti content in $\text{CaHf}_{1-y}\text{Ti}_y\text{X}_3$ ($\text{X} = \text{S}, \text{Se}$) alloys increases, the contribution of Ti-3d orbitals increases with respect to Hf-5d orbitals. The Ti-3d orbitals are more localized than the Hf-5d orbitals, so alloying with Ti lowers the energy of the CBM and reduces the bandgaps of these alloys.

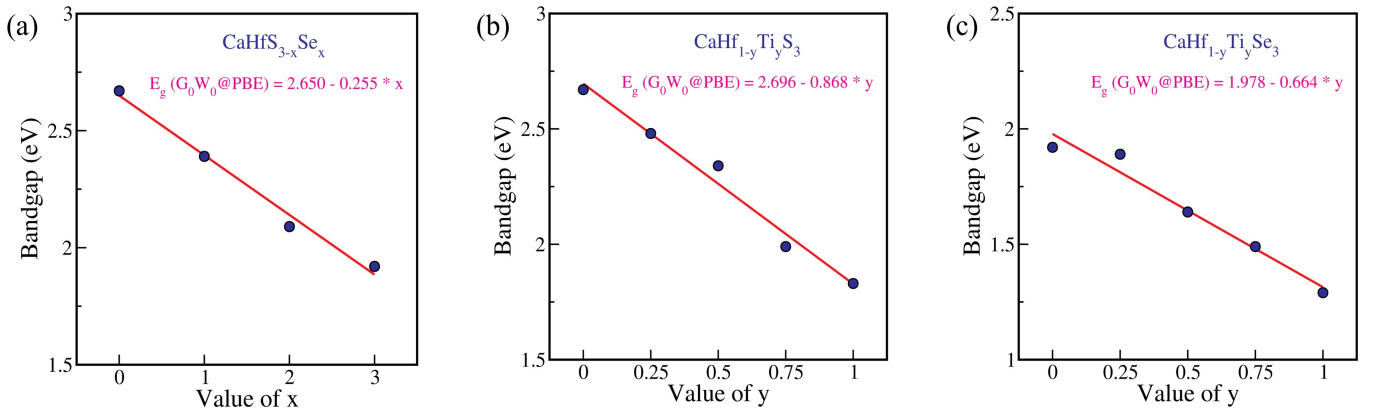


Figure 4. Variation of the calculated $G_0W_0@PBE$ bandgap with the value of x and y in (a) $CaHfS_{3-x}Se_x$, (b) $CaHf_{1-y}Ti_yS_3$, and (c) $CaHf_{1-y}Ti_ySe_3$ CPs.

Further, to gain a deep insight into charge carrier transport, we computed the effective masses of electrons (m_e^*) and holes (m_h^*) for all the investigated compounds by fitting the $E - k$ dispersion curves obtained from $G_0W_0@PBE$ band structures. The effective masses of these CPs are determined using the relation, $m^* = \hbar^2 [\partial^2 E(k)/\partial k^2]^{-1}$ and the corresponding values are presented in Table II. Note that, effective masses of the charge carriers are estimated along three different directions: $\Gamma-X$, $\Gamma-Y$, and $\Gamma-Z$, and then calculate their harmonic mean values using Eq. 2 (for details, see the Supplemental Material). From Table II, it is evident that m_e^* and m_h^* lie in the range of 0.162–0.552 and 0.103–0.380, respectively. These values suggest high ambipolar carrier mobility, which implies enhanced charge carrier transport in these materials.

C. Optical Properties:

To gain a comprehensive understanding of the suitability of a material for optoelectronic applications, an in-depth analysis of its optical properties, including the dielectric function and absorption coefficient, is indispensable. To enhance the reliability of our predictions, we have employed MBPT-based GW-BSE simulations, which explicitly incorporate electron-hole interactions. GW calculations determine the fundamental bandgap, which is considered more accurate and closely aligned with results from experimental photoelectron spectroscopy (PES) and inverse photoelectron spectroscopy (IPES) [35, 36]. On the other hand, BSE calculations predict the optical bandgap, providing results comparable to experimental optical absorption spectroscopy [37, 38]. To obtain the optical response of these CPs, a single-shot GW (G_0W_0) calculation is first performed based on the PBE functional. Following this, the Bethe-Salpeter equation (BSE) is solved using the $G_0W_0@PBE$ results. The optical response is assessed by calculating the frequency-dependent dielectric function, $\epsilon(\omega)$, expressed as $\epsilon(\omega) = [\text{Re}(\epsilon)] + i[\text{Im}(\epsilon)]$, where $[\text{Re}(\epsilon)]$ denotes the real part, and $[\text{Im}(\epsilon)]$ represents the imaginary part of the dielectric function.

The real part of the dielectric function, $[\text{Re}(\epsilon)]$, represents how a material responds to an electric field through polarization. Higher values of $[\text{Re}(\epsilon)]$ indicate stronger polarization, which influences the material's optical properties, including its refractive index and light absorption. The calculated $[\text{Re}(\epsilon)]$ of the investigated CPs obtained using $BSE@G_0W_0@PBE$ is depicted in Figure 5(a)-(c). Furthermore, the real part of the dielectric function $[\text{Re}(\epsilon)]$, at zero energy, is commonly referred to as the electronic or optical dielectric constant (ϵ_∞)—characterizes the dielectric screening effect during electron-hole Coulomb interactions. Our results show that the value of ϵ_∞ increases with the incorporation of Ti and Se in these CPs. This trend indicates reduced charge carrier recombination rates and improved optoelectronic performance in these materials, as a higher ϵ_∞ suggests stronger electronic screening and enhanced dielectric response. Notably, ϵ_∞ for $CaTiSe_3$ reaches 29.93, the highest among the studied compounds, highlighting its superior potential for optoelectronic applications.

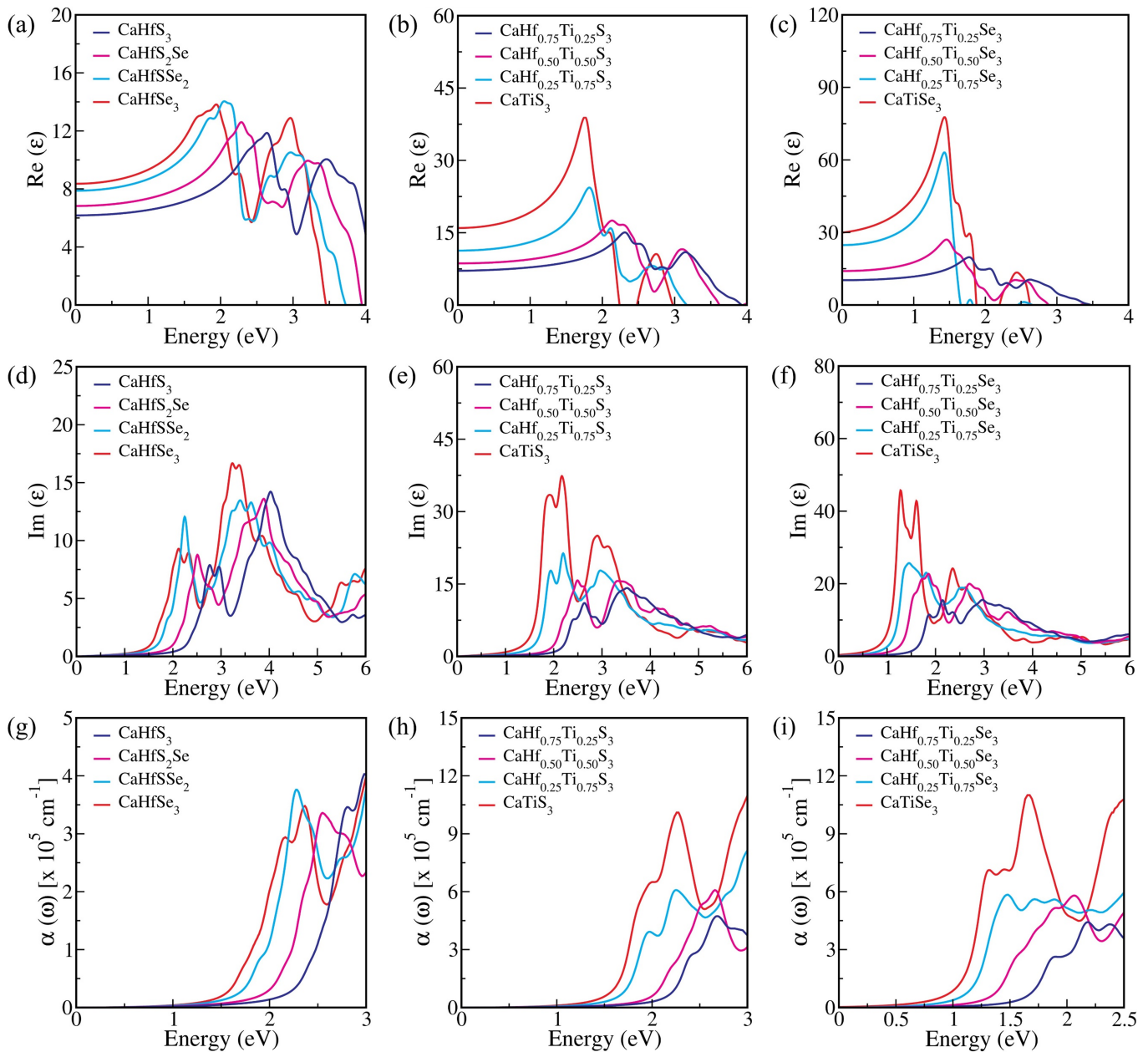


Figure 5. Real $[\text{Re}(\epsilon)]$ and imaginary $[\text{Im}(\epsilon)]$ part of the electronic dielectric function, and absorption coefficient $[\alpha(\omega)]$ of $\text{CaHfS}_{3-x}\text{Se}_x$ ($x = 0, 1, 2, 3$) and $\text{CaHf}_{1-y}\text{Ti}_y\text{X}_3$ ($y = 0, 0.25, 0.5, 0.75, 1$; $\text{X} = \text{S, Se}$) CPs, obtained using the BSE@ G_0W_0 @PBE method.

On the other hand, the imaginary part of the dielectric function, $[\text{Im}(\epsilon)]$, plays a key role in determining the linear absorption properties of a material. Figure 5(d)-(f) represents the $[\text{Im}(\epsilon)]$ of these CPs calculated using BSE@ G_0W_0 @PBE. It has been observed that both the absorption onset and the position of the first peak (E_o) of these CPs exhibit a gradual red shift with increasing concentrations of Ti and Se. This shift corresponds to a decrease in the quasiparticle (QP) bandgap, as detailed in Table II. For example, the E_o value for CaHfS_3 is 2.45 eV, whereas it decreases to 1.27 eV for CaTiSe_3 . It should be emphasized that these CPs exhibit an absorption onset from the near-infrared to the visible region, making them advantageous for solar cell applications.

One of the most crucial parameters for evaluating a material's suitability for photovoltaic applications is the absorption coefficient. This metric is essential for determining the material's potential for optimal solar energy conversion efficiency. Consequently, the absorption coefficient $[\alpha(\omega)]$ for each of the examined CPs is calculated using the following formula [39],

$$\alpha(\omega) = \sqrt{2}\omega \left[\sqrt{\{\text{Re}(\varepsilon)\}^2 + \{\text{Im}(\varepsilon)\}^2} - \text{Re}(\varepsilon) \right]^{1/2}. \quad (11)$$

Generally, a standard $\alpha(\omega)$ in the order of 10^5 cm^{-1} is preferred for direct semiconductors [18]. Based on our BSE@G₀W₀@PBE results, all of the studied perovskites meet this criterion [see Figure 5(g)-(i)], suggesting their potential for use in photovoltaic devices.

D. Excitonic Properties:

In addition to the optical properties, various excitonic parameters, including exciton binding energy (E_B), exciton radius (r_{exc}), and exciton lifetime (τ_{exc}), are also calculated for these perovskites. Excitons are bound states formed by an electron (e) and a hole (h) upon light absorption in a material, and the characteristics of these excitons significantly influence the photovoltaic performance of this material. The energy needed to separate an exciton into a free $e-h$ pair is called the exciton binding energy (E_B). In photovoltaics, a lower E_B promotes easier separation of $e-h$ pairs, which enhances photoelectric conversion efficiency. Theoretically, E_B is estimated from first-principles BSE calculations as the difference between the QP bandgap, E_g^d (direct G₀W₀@PBE bandgap), and the optical bandgap, E_o (first peak position from BSE@G₀W₀@PBE) [48, 52]. The E_B values, calculated using the first-principles BSE method for the systems under investigation, are shown in Table III, ranging from 0.016 to 0.221 eV. This indicates that these materials can achieve a comparable or even broader range of E_B values than conventional lead-based HPs (0.01–0.10 eV) [19–21]. The higher E_B values observed in some of our systems suggest substantial excitonic effects, which can be advantageous for applications requiring enhanced exciton binding, such as excitonic solar cells and light-emitting devices. Additionally, the ability to access both low and high E_B regimes offers tunability, making these materials versatile candidates for diverse optoelectronic applications. The E_B values of these CPs are also found to decrease with increasing Ti concentration, which can be attributed to higher electronic dielectric constants (ε_∞) and lower effective masses (see Equation 1).

In our study, Tables III and IV suggest that $E_B \gg \hbar\omega_{LO}$ for most of the systems, where ω_{LO} is the characteristic longitudinal optical phonon frequency. In this case, the electronic contribution to the dielectric screening dominates over the ionic contribution, allowing the ionic part to be neglected, which leads to no change in E_B [62, 63]. Further, the hydrogenic Wannier-Mott (WM) model [17, 18] is employed to determine the E_B for these mixed and alloyed perovskites using Eq. 1. In this model, ε_{eff} is positioned between the electronic (ε_∞) and static ($\varepsilon_{\text{static}} = \varepsilon_\infty + \varepsilon_{\text{ion}}$) dielectric constant, where ε_{ion} represents the ionic contribution to the dielectric function (for details, see the Supplemental Material). The values of ε_∞ and ε_{ion} are derived from the BSE and DFPT methods, respectively. The electronic and static dielectric constants establish the upper (E_{Bu}) and lower (E_{Bl}) bounds of exciton binding energy (for details, see the Supplemental Material). Our study also reveals that the upper bound values are smaller but align more closely with the E_B calculated using the standard BSE method than the lower bound values. Nevertheless, the overall trend remains consistent, indicating that the electronic contribution to dielectric screening is more prominent than the ionic contribution, and $\varepsilon_{\text{eff}} \rightarrow \varepsilon_\infty$ in these CPs.

Table III. Calculated excitonic parameters, phonon screening corrections (ΔE_B^{ph}), and modified exciton binding energy (E'_B) of chalcogenide perovskites.

Configurations	E_B (eV)	T_{exc} (K)	r_{exc} (nm)	$ \phi_n(0) ^2$ (10^{26} m^{-3})	ΔE_B^{ph} (meV)	E'_B (eV)
CaHfS ₃	0.221	2562	1.62	0.75	-16.60	0.204
CaHfS ₂ Se	0.183	2122	1.83	0.52	-15.42	0.168
CaHfSSe ₂	0.157	1820	2.51	0.20	-12.91	0.144
CaHfSe ₃	0.046	533	2.85	0.14	-9.90	0.036
CaHf _{0.75} Ti _{0.25} S ₃	0.133	1542	1.76	0.58	-15.70	0.117
CaHf _{0.75} Ti _{0.25} Se ₃	0.063	730	3.46	0.08	-10.89	0.052
CaHf _{0.50} Ti _{0.50} S ₃	0.116	1345	2.46	0.21	-15.17	0.101
CaHf _{0.50} Ti _{0.50} Se ₃	0.059	684	5.84	0.02	-10.27	0.049
CaHf _{0.25} Ti _{0.75} S ₃	0.080	928	3.66	0.06	-14.85	0.065
CaHf _{0.25} Ti _{0.75} Se ₃	0.051	591	12.97	0.001	-9.59	0.041
CaTiS ₃	0.022	255	6.98	0.009	-11.48	0.011
CaTiSe ₃	0.016	186	25.13	0.0002	-7.85	0.008

Using the aforementioned quantities (E_B , ε_∞ , and μ^*), several excitonic parameters are also computed, including excitonic temperature (T_{exc}), radius (r_{exc}), and probability of wave function ($|\phi_n(0)|^2$) for $e-h$ pair at zero separation.

T_{exc} represents the maximum temperature at which an exciton remains stable, and the thermal energy needed to separate an exciton is given by $E_B = k_B T_{exc}$, where k_B is the Boltzmann constant. Furthermore, r_{exc} and $|\phi_n(0)|^2$ are calculated using Eqs. 5 and 6, respectively. The values of these parameters are listed in Table III, and the inverse of $|\phi_n(0)|^2$ can be used to qualitatively characterize the exciton lifetime (τ_{exc} ; for details, see the Supplemental Material). Table III indicates that the τ_{exc} values for the investigated CPs increase with the rising concentration of Ti in conjunction with Se. A longer exciton lifetime is associated with a lower carrier recombination rate, which improves the quantum yield and conversion efficiency.

Our results show that the upper bound values of E_B , estimated using the WM model, are smaller but more closely aligned with the E_B values calculated using the standard BSE method. One reason is that the standard BSE (ab initio) approach considers only electronic screening when constructing the $e-h$ kernel for calculating the E_B . However, static screening does not account for electron-phonon coupling, which can be crucial in certain materials, particularly those with significant electron-phonon interactions or where phonons are key to determining optoelectronic properties. In a recent study, Filip and colleagues [50] incorporated phonon screening into E_B by considering four distinct material parameters: μ^* , ε_∞ , ε_{static} , and ω_{LO} . The phonon-screening correction (ΔE_B^{ph}), assuming isotropic and parabolic electronic band dispersion, is computed through Eq. 4, with the corresponding values for these compounds provided in Table III. The contribution of phonon screening is found to reduce E_B by 7.85 meV to 16.60 meV, which is significant for certain materials and, therefore, cannot be overlooked. After incorporating the phonon-screening correction, the modified exciton binding energy (E'_B) ranges from 0.008 to 0.204 eV, indicating that these perovskite alloys are promising materials for photovoltaic applications.

E. Polaronic Properties:

To further enhance our understanding of the fundamental limits of carrier mobility for these CPs, it would be advantageous to make predictions based on first-principles calculations [25, 64]. In polar semiconductors, the scattering mechanism near room temperature is dominated by the interaction between charge carriers and the macroscopic electric field generated by longitudinal optical (LO) phonons [18, 52]. Therefore, when calculating the mobility using theoretical approaches, it is crucial to consider the polaron state, which arises from the strong interactions between charge carriers and phonons, rather than focusing solely on the free carrier state. Fröhlich formulated a Hamiltonian to describe the interaction between independent charge carriers (i.e., those with low density) and polar optical phonons [65]. This interaction is characterized by the dimensionless Fröhlich parameter, α , as defined in Eq. 7. The computed carrier-phonon coupling constants (α) are listed in Table IV. Strong carrier-phonon coupling is typically indicated by $\alpha > 10$, whereas $\alpha \ll 1$ usually suggests weak coupling [25]. Our results indicate that the polaron in these materials resides in the weak to intermediate coupling regime ($\alpha = 0.34-2.68$). In our study, $\text{CaHf}_{0.25}\text{Ti}_{0.75}\text{Se}_3$ and CaTiSe_3 exhibit smaller electron-phonon coupling relative to the other materials. The reduced carrier-phonon coupling can be ascribed to factors such as a lower effective mass of the carriers and a higher electronic dielectric constant. Additionally, the Debye temperature (θ_D) for these CPs is calculated and found to be lower than room temperature (see Table IV), indicating a significant interaction between carriers and phonons.

Polaron formation refers to the interaction of a charge carrier (electron or hole) with its surrounding lattice, causing a local distortion. This interaction can reduce the QP energies, meaning that both electrons and holes lose energy when forming polarons. The polaron energy (E_p) can be determined from α using Eq. 8. The QP gap, arising from the polaron energy of electrons and holes (see Table IV), is also computed and compared with the E_B from Table III. From this comparison, we observe that, for the investigated CPs, the energy of charge-separated polaronic states is lower than that of bound exciton states, except in the cases of CaHfSe_3 and CaTiS_3 . For example, the QP gap of $\text{CaHf}_{0.25}\text{Ti}_{0.75}\text{Se}_3$ is 12.49 meV, while the E_B value for this compound is 51 meV. This suggests that in most systems, charge-separated polaronic states (where electrons and holes are further apart) are less stable than bound excitons (where they remain closely associated).

Table IV. Polaron parameters for electrons (e) and holes (h) in chalcogenide perovskites.

Configurations	ω_{LO} (THz)	θ_D (K)	α		E_p (meV)		m_p/m^*		μ_p ($\text{cm}^2\text{V}^{-1}\text{s}^{-1}$)	
			e	h	e	h	e	h	e	h
CaHfS ₃	5.14	247	2.22	2.08	48.55	45.41	1.49	1.46	27.83	34.59
CaHfS ₂ Se	4.91	236	1.99	1.87	41.45	38.90	1.43	1.40	33.84	41.78
CaHfSSe ₂	4.15	199	1.72	1.59	30.19	27.86	1.36	1.33	51.02	65.94
CaHfSe ₃	3.55	170	1.76	1.54	26.43	23.07	1.37	1.31	53.60	82.70
CaHf _{0.75} Ti _{0.25} S ₃	4.39	211	2.68	2.13	50.33	39.74	1.63	1.47	17.70	39.09
CaHf _{0.75} Ti _{0.25} Se ₃	3.22	155	1.91	1.42	26.07	19.27	1.41	1.29	40.80	107.60
CaHf _{0.50} Ti _{0.50} S ₃	4.24	204	2.07	1.70	37.27	30.47	1.45	1.36	30.93	59.47
CaHf _{0.50} Ti _{0.50} Se ₃	2.90	139	1.36	1.04	16.61	12.65	1.27	1.20	83.76	308.68
CaHf _{0.25} Ti _{0.75} S ₃	5.14	247	1.16	0.95	25.04	20.46	1.23	1.18	68.39	123.99
CaHf _{0.25} Ti _{0.75} Se ₃	3.80	182	0.45	0.34	7.12	5.37	1.08	1.06	482.16	1026.68
CaTiS ₃	4.63	222	0.78	0.72	15.10	13.93	1.15	1.13	172.02	221.38
CaTiSe ₃	2.90	139	0.43	0.34	5.19	4.12	1.08	1.06	668.29	1271.42

Feynman developed an innovative approach to solve the Fröhlich Hamiltonian, describing the interaction between an electron and a collection of independent phonon excitations, which behave harmonically and are incorporated into the quantum field theory [53]. As the electron moves through the lattice, it interacts with the perturbation it creates, which diminishes exponentially over time. Using Feynman’s method, the effective mass of the polaron (m_p) for our systems is also calculated following Eq. 9 and the values are tabulated in Table IV. These results reveal that electron-phonon coupling leads to an increase in the polaron effective mass by 6–63%, confirming weak to intermediate carrier-lattice interactions.

Furthermore, the polaron mobility is estimated using the Hellwarth polaron model through Eq. 10 to confirm the impact of the increasing polaron effective mass. Polaron mobility quantifies how easily a polaron moves through a lattice, influenced by its effective mass and the strength of carrier-lattice interactions. As the polaron’s effective mass increases due to stronger electron-phonon coupling, the mobility generally decreases, causing the polaron to move more slowly within the material. This trend is also evident in our systems of interest (see Table IV). However, interestingly, mobility is found to increase with the increase in Ti concentration, and it boosts significantly in the presence of Se. Notably, these materials display ambipolar characteristics in polaron mobility, with values ranging from 17.70 to 668.29 $\text{cm}^2\text{V}^{-1}\text{s}^{-1}$ for electrons and 34.59 to 1271.42 $\text{cm}^2\text{V}^{-1}\text{s}^{-1}$ for holes. The mobility values of these alloyed Ti-rich Se-based perovskites are substantially higher than those found in conventional lead-based HPs (57–290 $\text{cm}^2\text{V}^{-1}\text{s}^{-1}$ for electrons and 97–230 $\text{cm}^2\text{V}^{-1}\text{s}^{-1}$ for holes, respectively) [23, 25]. Overall, the polaronic properties suggest that doping at both cationic and anionic sites enhances photovoltaic performance in these systems.

F. Spectroscopic Limited Maximum Efficiency:

As discussed, these alloyed perovskites exhibit a high absorption coefficient and a direct bandgap within the optimal range, making them promising candidates for efficient solar absorbers. To further evaluate the photovoltaic performance of these materials, the spectroscopic limited maximum efficiency (SLME), as introduced by Yu and Zunger [66], is also calculated (for details, see the Supplemental Material). SLME is an improved performance metric over the Shockley-Queisser (SQ) efficiency limit [67], specifically designed to assess the theoretical maximum efficiency of a thin-film absorber material. The latter is less realistic as it overlooks losses from radiative recombination caused by the non-conservation of absorbed photon momentum. The SLME model considers various factors, including the magnitude and nature (direct or indirect) of the bandgap, the shape of the absorption spectrum, the absorber layer thickness, the material-specific non-radiative recombination losses, and the temperature. Therefore, the theoretical SLME of our investigated perovskites is evaluated at 293.15 K using the standard solar spectrum (AM1.5G), along with the absorption coefficient, material thickness, and the electronic G_0W_0 @PBE bandgap as input parameters.

To perform the SLME calculation, we first assess the optical transition possibility from VBM to CBM in these compounds. It has been observed that, despite having a direct electronic bandgap, the optically allowed dipole transition from VBM to CBM can still be forbidden in some perovskites [14, 18]. This is due to the inversion symmetry in these structures, which results in the VBM and CBM having the same parity. To confirm the possibility of optical transitions from the VBM to the CBM in our investigated systems, the transition dipole moment matrix element (P) is computed, since its square (P^2) determines the transition probability between the initial (VBM) and final (CBM) states. The P^2 values for each system are plotted and shown in Figure 6(a) and Figure S1, below their respective G_0W_0 @PBE band structure plots. These results indicate that all the compounds exhibit allowed dipole transitions at the Γ point. Note that CaTiSe₃ has an indirect electronic bandgap but exhibits an optically allowed dipole transition

at its lowest direct band edge. For this indirect bandgap material, non-radiative recombination significantly influences the SLME calculation. Meanwhile, radiative recombination is modulated by a factor $f_r = e^{(E_g - E_g^{da})/k_B T}$, where E_g is the fundamental bandgap, E_g^{da} is the direct allowed bandgap, k_B is the Boltzmann constant, and T is the temperature [66] (for details, see the Supplemental Material).

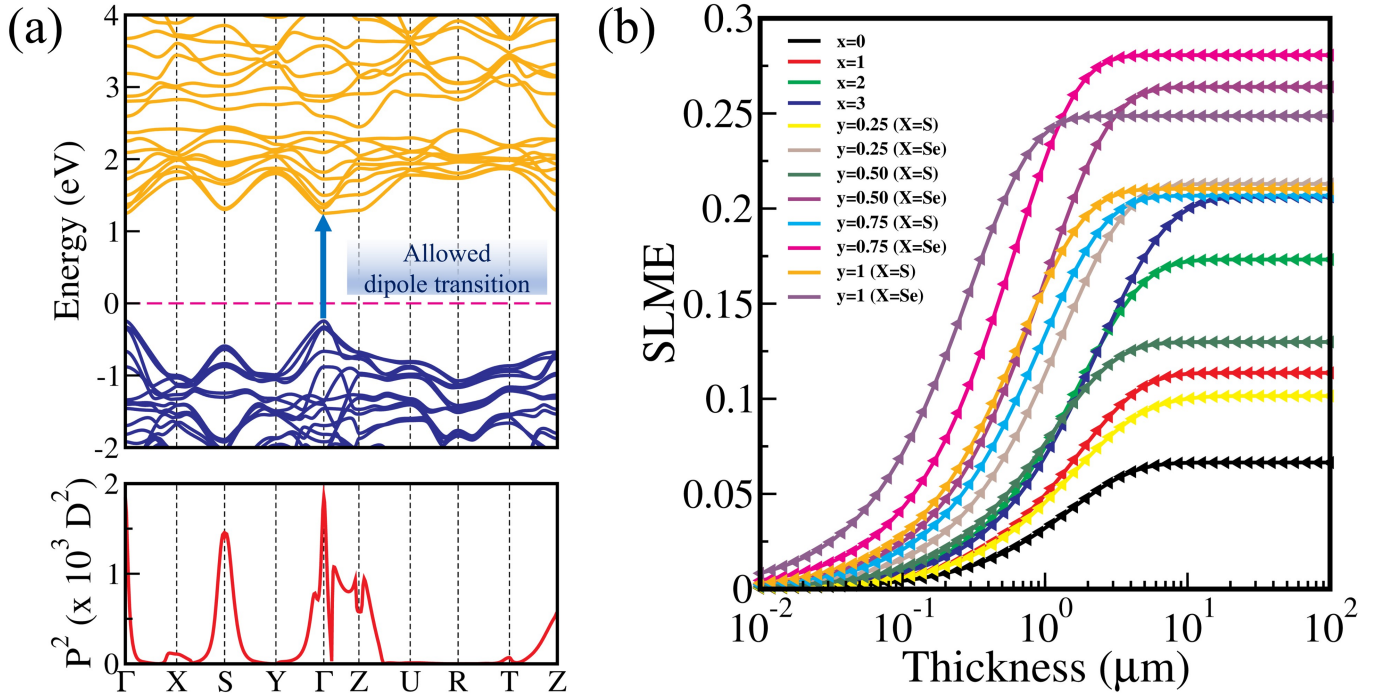


Figure 6. (a) Electronic band structure and transition probability (square of the transition dipole moment matrix elements) of $\text{CaHf}_{0.25}\text{Ti}_{0.75}\text{Se}_3$ perovskite calculated using $G_0W_0@PBE$ method, and (b) spectroscopic limited maximum efficiency of $\text{CaHfS}_{3-x}\text{Se}_x$ ($x = 0, 1, 2, 3$) and $\text{CaHf}_{1-y}\text{Ti}_y\text{X}_3$ ($y = 0.25, 0.5, 0.75, 1$; $X = \text{S, Se}$) CPs calculated using $BSE@G_0W_0@PBE$ method.

Next, the thickness dependence SLME calculations are conducted for all the investigated compounds using $BSE@G_0W_0@PBE$ method, as shown in Figure 6(b). It is found that the SLME of these materials increases with thickness up to a certain point, after which it levels off. The maximum SLME values of these CPs at a $10 \mu\text{m}$ absorber layer thickness are found in the range of 6.65%–28.06%. Among these compounds, $\text{CaHf}_{0.25}\text{Ti}_{0.75}\text{Se}_3$ exhibits the highest SLME of 28.06% at a thickness of $3 \mu\text{m}$, which is very close to the maximum SLME of $\text{CH}_3\text{NH}_3\text{PbI}_3$ (28.97% at $2 \mu\text{m}$ thickness) [22]. Our SLME results demonstrate that doping at both the cationic and anionic sites substantially improves the photovoltaic potential of the studied systems. Overall, these doped CP alloys emerge as more promising candidates for photovoltaic applications compared to pristine CsPbI_3 , ABX_3 ($A = \text{Ca, Sr, Ba}$; $B = \text{Zr, Hf}$, and $X = \text{S, Se}$), and other halide perovskites [14, 17, 18, 24, 68–70].

IV. CONCLUSION:

In this work, we conducted a deep dive into the electronic, optical, excitonic, and polaronic properties of alloyed chalcogenide perovskites— $\text{CaHfS}_{3-x}\text{Se}_x$ ($x = 0, 1, 2, 3$) and $\text{CaHf}_{1-y}\text{Ti}_y\text{X}_3$ ($y = 0, 0.25, 0.50, 0.75, 1$; $X = \text{S, Se}$)—using cutting-edge first-principles based simulations. Phonon dispersion curves and elastic properties confirm these materials are rock-solid. Our electronic structure analysis reveals direct $G_0W_0@PBE$ bandgaps between 1.29–2.67 eV, coupled with low carrier effective masses, signaling exceptional ambipolar mobility. Optical properties, calculated via the Bethe-Salpeter equation, show an intense absorption onset stretching from the near-infrared to the visible spectrum, making them perfect for solar harvesting. Exciton binding energy drops (0.008–0.204 eV), while exciton lifetimes extend with Ti and Se alloying—unlocking more excellent photophysical performance. Polaron analysis adds another layer of promise: weak-to-intermediate carrier-phonon coupling, with charge-carrier mobilities reaching staggering levels—up to $668.29 \text{ cm}^2\text{V}^{-1}\text{s}^{-1}$ for electrons and $1271.42 \text{ cm}^2\text{V}^{-1}\text{s}^{-1}$ for holes, for the Ti-rich Se-based perovskites—far outshining conventional lead-based and pristine chalcogenide perovskites. Our theoretical efficiency

estimates hit a game-changing 28.06%, positioning these materials as frontrunners for lead-free, high-efficiency photovoltaic devices. Alloyed chalcogenide perovskites may rewrite the rules for next-gen optoelectronics—brighter, faster, and more sustainable than ever before.

ACKNOWLEDGMENTS

The authors would like to acknowledge the Council of Scientific and Industrial Research (CSIR), Government of India [Grant No. 3WS(007)/2023-24/EMR-II/ASPIRE] for financial support. S.A. would like to acknowledge the Council of Scientific and Industrial Research (CSIR), Government of India [Grant No. 09/1128(11453)/2021-EMR-I] for Senior Research Fellowship. The authors acknowledge the High Performance Computing Cluster (HPCC) ‘Magus’ at Shiv Nadar Institution of Eminence for providing computational resources that have contributed to the research results reported within this paper.

-
- [1] A. Kojima, K. Teshima, Y. Shirai, and T. Miyasaka, *J. Am. Chem. Soc.* **131**, 6050 (2009), <https://doi.org/10.1021/ja809598r>.
 - [2] N.-G. Park, *J. Phys. Chem. Lett.* **4**, 2423 (2013), <https://doi.org/10.1021/jz400892a>.
 - [3] J. Berry, T. Buonassisi, D. A. Egger, G. Hodes, L. Kronik, Y.-L. Loo, I. Lubomirsky, S. R. Marder, Y. Mastai, J. S. Miller, D. B. Mitzi, Y. Paz, A. M. Rappe, I. Riess, B. Rybtchinski, O. Stafsudd, V. Stevanovic, M. F. Toney, D. Zitoun, A. Kahn, D. Ginley, and D. Cahen, *Adv. Mater.* **27**, 5102 (2015), <https://onlinelibrary.wiley.com/doi/pdf/10.1002/adma.201502294>.
 - [4] D. A. Egger, A. M. Rappe, and L. Kronik, *Acc. Chem. Res.* **49**, 573 (2016), <https://doi.org/10.1021/acs.accounts.5b00540>.
 - [5] NREL, Photovoltaic Research (2024).
 - [6] D. B. Straus, S. Guo, A. M. Abeykoon, and R. J. Cava, *Adv. Mater.* **32**, 2001069 (2020), <https://onlinelibrary.wiley.com/doi/pdf/10.1002/adma.202001069>.
 - [7] A. Babayigit, A. Ethirajan, M. Muller, and B. Conings, *Nat. Mater.* **15**, 247 (2016).
 - [8] D. Tiwari, O. S. Hutter, and G. Longo, *J. Phys. Energy* **3**, 034010 (2021).
 - [9] S. Niu, H. Huyan, Y. Liu, M. Yeung, K. Ye, L. Blankemeier, T. Orvis, D. Sarkar, D. J. Singh, R. Kapadia, and J. Ravichandran, *Adv. Mater.* **29**, 1604733 (2017), <https://onlinelibrary.wiley.com/doi/pdf/10.1002/adma.201604733>.
 - [10] X. Wu, W. Gao, J. Chai, C. Ming, M. Chen, H. Zeng, P. Zhang, S. Zhang, and Y.-Y. Sun, *Sci. China Mater.* **64**, 2976 (2021).
 - [11] Y.-Y. Sun, M. L. Agiorgousis, P. Zhang, and S. Zhang, *Nano Lett.* **15**, 581 (2015), <https://doi.org/10.1021/nl504046x>.
 - [12] D. Liu, H. Zeng, H. Peng, and R. Sa, *Phys. Chem. Chem. Phys.* **25**, 13755 (2023).
 - [13] A. Swarnkar, W. J. Mir, R. Chakraborty, M. Jagadeeswararao, T. Sheikh, and A. Nag, *Chem. Mater.* **31**, 565 (2019), <https://doi.org/10.1021/acs.chemmater.8b04178>.
 - [14] P. Basera and S. Bhattacharya, *J. Phys. Chem. Lett.* **13**, 6439 (2022), <https://doi.org/10.1021/acs.jpcclett.2c01337>.
 - [15] R. Lelieveld and D. J. W. IJdo, *Acta Cryst. B* **36**, 2223 (1980).
 - [16] T. Fix, S. Raissi, D. Muller, C. Bouillet, D. Preziosi, and A. Slaoui, *J. Alloys Compd.* **964**, 171272 (2023).
 - [17] M. Kumar, A. Singh, D. Gill, and S. Bhattacharya, *J. Phys. Chem. Lett.* **12**, 5301 (2021).
 - [18] S. Adhikari and P. Johari, *Phys. Rev. B* **109**, 174114 (2024).
 - [19] H. M. Ghaithan, S. M. H. Qaid, Z. A. Alahmed, M. Hezam, A. Lyras, M. Amer, and A. S. Aldwayyan, *J. Phys. Chem. C* **125**, 886 (2021), <https://doi.org/10.1021/acs.jpcc.0c07983>.
 - [20] R. Comin, G. Walters, E. S. Thibau, O. Voznyy, Z.-H. Lu, and E. H. Sargent, *J. Mater. Chem. C* **3**, 8839 (2015).
 - [21] X. Chen, H. Lu, Y. Yang, and M. C. Beard, *J. Phys. Chem. Lett.* **9**, 2595 (2018), PMID: 29714488, <https://doi.org/10.1021/acs.jpcclett.8b00526>.
 - [22] Q. Sun, H. Chen, and W.-J. Yin, *Chem. Mater.* **31**, 244 (2019), <https://doi.org/10.1021/acs.chemmater.8b04320>.
 - [23] Y. Kang and S. Han, *Phys. Rev. Appl.* **10**, 044013 (2018).
 - [24] H. Zou, Y. Duan, S. Yang, D. Xu, L. Yang, J. Cui, H. Zhou, M. Wu, J. Wang, X. Lei, N. Zhang, and Z. Liu, *Small* **19**, 2206205 (2023), <https://onlinelibrary.wiley.com/doi/pdf/10.1002/smll.202206205>.
 - [25] J. M. Frost, *Phys. Rev. B* **96**, 195202 (2017).
 - [26] W. Meng, B. Saparov, F. Hong, J. Wang, D. B. Mitzi, and Y. Yan, *Chem. Mater.* **28**, 821 (2016), <https://doi.org/10.1021/acs.chemmater.5b04213>.
 - [27] S. Kong, H. Dong, Z. Yu, J. Guo, K. Cao, K. Chen, X. Ke, C. Zhou, J. Deng, S. Yang, and Y. Zhang, *Ceram. Int.* **50**, 10889 (2024).
 - [28] R. Chami, A. Lekdadri, L. Omari, E. Hlil, and M. Chafi, *Mater. Today Energy* **20**, 100689 (2021).
 - [29] R. Chami, A. Lekdadri, M. Chafi, L. Omari, and E. Hlil, *Solid State Commun.* **369**, 115212 (2023).
 - [30] D. Liu, H. Peng, J. He, and R. Sa, *Mater. Sci. Semicond. Process.* **169**, 107919 (2024).
 - [31] P. Hohenberg and W. Kohn, *Phys. Rev.* **136**, B864 (1964).
 - [32] W. Kohn and L. J. Sham, *Phys. Rev.* **140**, A1133 (1965).
 - [33] H. Jiang, P. Rinke, and M. Scheffler, *Phys. Rev. B* **86**, 125115 (2012).

- [34] F. Fuchs, C. Rödl, A. Schleife, and F. Bechstedt, *Phys. Rev. B* **78**, 085103 (2008).
- [35] L. Hedin, *Phys. Rev.* **139**, A796 (1965).
- [36] M. S. Hybertsen and S. G. Louie, *Phys. Rev. Lett.* **55**, 1418 (1985).
- [37] S. Albrecht, L. Reining, R. Del Sole, and G. Onida, *Phys. Rev. Lett.* **80**, 4510 (1998).
- [38] M. Rohlfling and S. G. Louie, *Phys. Rev. Lett.* **81**, 2312 (1998).
- [39] M. Gajdoš, K. Hummer, G. Kresse, J. Furthmüller, and F. Bechstedt, *Phys. Rev. B* **73**, 045112 (2006).
- [40] G. Kresse and J. Furthmüller, *Phys. Rev. B* **54**, 11169 (1996).
- [41] G. Kresse and J. Furthmüller, *Comput. Mater. Sci.* **6**, 15 (1996).
- [42] P. E. Blöchl, *Phys. Rev. B* **50**, 17953 (1994).
- [43] J. P. Perdew, K. Burke, and M. Ernzerhof, *Phys. Rev. Lett.* **77**, 3865 (1996).
- [44] K. Momma and F. Izumi, *J. Appl. Crystallogr.* **44**, 1272 (2011).
- [45] A. Togo, L. Chaput, T. Tadano, and I. Tanaka, *J. Phys. Condens. Matter* **35**, 353001 (2023).
- [46] J. Heyd, G. E. Scuseria, and M. Ernzerhof, *J. Chem. Phys.* **118**, 8207 (2003).
- [47] V. Wang, N. Xu, J.-C. Liu, G. Tang, and W.-T. Geng, *Comput. Phys. Commun.* **267**, 108033 (2021).
- [48] S. Adhikari and P. Johari, *Phys. Rev. Mater.* **7**, 075401 (2023).
- [49] J. Kangsabanik, M. K. Svendsen, A. Taghizadeh, A. Crovetto, and K. S. Thygesen, *J. Am. Chem. Soc.* **144**, 19872 (2022), PMID: 36270007, <https://doi.org/10.1021/jacs.2c07567>.
- [50] M. R. Filip, J. B. Haber, and J. B. Neaton, *Phys. Rev. Lett.* **127**, 067401 (2021).
- [51] R. W. Hellwarth and I. Biaggio, *Phys. Rev. B* **60**, 299 (1999).
- [52] S. Adhikari and P. Johari, *Phys. Rev. B* **110**, 014101 (2024).
- [53] R. P. Feynman, *Phys. Rev.* **97**, 660 (1955).
- [54] J. Xu, J.-B. Liu, J. Wang, B.-X. Liu, and B. Huang, *Adv. Funct. Mater.* **28**, 1800332 (2018).
- [55] C. Li, X. Lu, W. Ding, L. Feng, Y. Gao, and Z. Guo, *Acta Crystallogr.* **64**, 702 (2008).
- [56] G. Volonakis, A. A. Haghighirad, R. L. Milot, W. H. Sio, M. R. Filip, B. Wenger, M. B. Johnston, L. M. Herz, H. J. Snaith, and F. Giustino, *J. Phys. Chem. Lett.* **8**, 772 (2017).
- [57] F. Mouhat and F.-X. Coudert, *Phys. Rev. B* **90**, 224104 (2014).
- [58] Z.-j. Wu, E.-j. Zhao, H.-p. Xiang, X.-f. Hao, X.-j. Liu, and J. Meng, *Phys. Rev. B* **76**, 054115 (2007).
- [59] R. Hill, *Proc. Phys. Soc. A* **65**, 349 (1952).
- [60] S. Pugh, London, *Edinburgh Dublin Philos. Mag. J. Sci.* **45**, 823 (1954).
- [61] X. Wei, H. Hui, S. Perera, A. Sheng, D. F. Watson, Y.-Y. Sun, Q. Jia, S. Zhang, and H. Zeng, *ACS Omega* **5**, 18579 (2020), <https://doi.org/10.1021/acsomega.0c00740>.
- [62] M. Bokdam, T. Sander, A. Stroppa, S. Picozzi, D. D. Sarma, C. Franchini, and G. Kresse, *Sci. Rep.* **6**, 28618 (2016).
- [63] C. D. Spataru and F. Leonard, *Chem. Phys.* **413**, 81 (2013).
- [64] L. M. Herz, *ACS Energy Lett.* **2**, 1539 (2017), <https://doi.org/10.1021/acseenergylett.7b00276>.
- [65] H. Fröhlich, *Adv. Phys.* **3**, 325 (1954), <https://doi.org/10.1080/00018735400101213>.
- [66] L. Yu and A. Zunger, *Phys. Rev. Lett.* **108**, 068701 (2012).
- [67] W. Shockley and H. J. Queisser, *J. Appl. Phys.* **32**, 510 (2004), https://pubs.aip.org/aip/jap/article-pdf/32/3/510/10548356/510_1_online.pdf.
- [68] A. C. Dias, M. P. Lima, and J. L. F. Da Silva, *J. Phys. Chem. C* **125**, 19142 (2021), <https://doi.org/10.1021/acs.jpcc.1c05245>.
- [69] J. Qian, B. Xu, and W. Tian, *Org. Electron.* **37**, 61 (2016).
- [70] J. Kangsabanik, V. Sugathan, A. Yadav, A. Yella, and A. Alam, *Phys. Rev. Mater.* **2**, 055401 (2018).